Biosensors and Bioelectronics: X 29 (2026) 100755

Contents lists available at ScienceDirect

Biosensors and Bioelectronics: X

journal homepage: www.journals.elsevier.com/biosensors-and-bioelectronics-x

A reliable high-throughput OECT-based bioelectronic system enabling pan-specific vesicle quantification

Giulia Frusconi [a], Angelo Musicò [b,c], Andrea Zendrini [b,c], Zsolt M. Kovács-Vajna [a], Lucia Paolini [b,c], Paolo Bergese [b,c], Fabrizio Torricelli [a,*]

[a] Department of Information Engineering, University of Brescia, Via Branze 38, 25123, Brescia, Italy
[b] Department of Molecular and Translational Medicine, University of Brescia, Viale Europa 11, 25121, Brescia, Italy
[c] CSGI - Center for Colloid and Interface Science, Firenze, Italy

ARTICLE INFO

Keywords:
Bioelectronic system
Organic electrochemical transistors
Total vesicle quantification
Click chemistry
Organic bioelectronics

ABSTRACT

Next-generation extracellular vesicle (EV) technologies are transforming biomanufacturing and functional product development. Quantifying EVs based on their membrane protein content is crucial for ensuring consistent yield, composition, and functional performance in manufacturing pipelines. Existing methods measure EV size and concentration but provide no information on membrane protein presence, whereas immunoaffinity approaches depend on specific markers that may be inconsistently expressed due to EV heterogeneity. Here we demonstrate a reliable bioelectronic system for pan-specific, high-throughput total EV quantification, achieving 12 independent parallel analysis in less than 15 min, with false-positive and false-negative rates below 1%. The system features multiple channel-functionalized arrays of organic electrochemical transistors (OECTs) in a 3×4 matrix configuration. Click chemistry enables real-time detection of EVs with membrane proteins, with a limit of identification of 6×10^6 particles ml^{-1} and a dynamic range spanning three orders of magnitude. By integrating functionalized OECT arrays with 3D-printed fluidic devices into a low-cost, disposable cartridge operated by a compact silicon-based electronic reader, the system enables rapid, reliable, and pan-specific total EV quantification in a user-friendly format, opening opportunities for in-line quality control and scalable implementation in biomanufacturing and pharmaceutical processes.

1. Introduction

Drug delivery is undergoing a paradigm shift, moving from synthetic nanocarriers toward biologically derived systems. Among these, extracellular vesicles (EVs) have emerged as nature's own delivery vehicles, uniquely combining therapeutic potential with intrinsic biocompatibility. Their endogenous origin provides advantages such as immune tolerance, reduced clearance, and efficient barrier crossing, underpinning their growing use in drug delivery strategies (Herrmann et al., 2021a; Tenchov et al., 2022). EVs are lipid bilayer-enclosed nanoparticles, typically ranging from 30 to 1000 nm, released by virtually all cell types into body fluids, and carry proteins, nucleic acids, and lipids (Welsh et al., 2024).

The promise of EVs as next-generation drug delivery platforms has spurred significant commercial interest. The market for EV therapeutics is projected to grow from USD 55 billion in 2022 to almost USD 2 trillion by 2030 (Lee, 2024), highlighting both the scientific potential and the need for robust and scalable manufacturing pipelines. The choice of cellular source is a critical first step in EV manufacturing, as it determines vesicle yield, composition, and scalability for therapeutic applications. Among potential sources, human red blood cells (RBCs) stand out, due to their long-standing clinical use in blood transfusions, which demonstrates both safety and minimal risk of horizontal gene transfer (Nguyen et al., 2023; Xu et al., 2021). For example, the delivery of RBC-derived EVs (RBCEVs) loaded with paclitaxel has demonstrated significant enhancement in drug efficacy, suppressing tumor growth in lung cancer models, both in vitro and in vivo, at clinically relevant doses, without observable toxicity or oncogenesis risk (Pham et al., 2021). Moreover, the ready availability of RBCs from donors or patients facilitates scalable and reproducible vesicle production, allowing controlled isolation and purification within a manufacturing workflow (Usman et al., 2018). In addition to RBCs, other promising EV sources are under investigation. Immune cells and bacteria are being explored for applications such as cancer vaccines (Bhatta et al., 2023), offering

* Corresponding author.
E-mail address: fabrizio.torricelli@unibs.it (F. Torricelli).

https://doi.org/10.1016/j.biosx.2026.100755
Received 7 November 2025; Received in revised form 17 January 2026; Accepted 1 February 2026
Available online 6 February 2026

the potential for targeted immunomodulation and therapeutic specificity, while milk-(Qu et al., 2025) or plant-derived (J. Feng et al., 2023) EVs provide abundant, easily cultivated material suitable for high-volume, cost-effective production, making them attractive for scalable therapeutic manufacturing. With the cellular source established, transforming EVs into therapeutic-grade products involves a multi-step manufacturing pipeline. Cargo is introduced in isolated and purified EVs via electroporation, sonication, freeze-thaw cycling, or chemical conjugation (Ahmed et al., 2024; Armstrong et al., 2017; Ciferri et al., 2024; Xu et al., 2021). Subsequent purification removes unincorporated material, yielding a formulation suspended in a physiologic or sterile buffer optimized for stability, storage, and clinical administration. Despite their effectiveness, these engineering steps inherently reduce intact vesicle number and may alter membrane protein display and biodistribution patterns, creating heterogeneity within each batch that can compromise downstream quantification and functional assessment (Xiang et al., 2025; Xu et al., 2025). For instance, electroporation and sonication can temporarily permeabilize the EV membrane, facilitating cargo entry but also potentially leading to membrane protein perturbation or disruption (Armstrong et al., 2017; Deshmukh et al., 2021). EV membrane proteins act as a "barcode", providing a unique signature that allows targeted delivery to specific cells or tissues, whether locally or systemically. Therefore, monitoring membrane protein integrity and vesicle abundance, can deliver a rapid feedback that allows interventions before the process is completed ensuring vesicles quality criteria through the pipeline (Herrmann et al., 2021b; Lee, 2024; Wang et al., 2023; Xu et al., 2025).

Currently, nanoparticle tracking analysis (NTA) serves as the gold standard for EV quantification, using laser light scattering to monitor Brownian motion in liquid media. While NTA offers high sensitivity, broad dynamic range (10^7 to 10^9 particles per milliliter), and could be adapted for in-line applications, it quantifies EVs based solely on size and shape, providing no information on the presence of membrane proteins, which are critical for vesicle functionality and quality assessment (Comfort et al., 2021). Conventional protein-based methods, such as immunosorbent assays and flow cytometry (FCM), quantify EVs via surface markers like the widely used tetraspanins (e.g., CD9, CD63, CD81). In diagnostic contexts, these methods exploit well-characterized EV markers to identify vesicles from specific cell types or pathological conditions, enabling precise detection of clinically relevant subpopulations (Hendrix et al., 2023; Spitzberg et al., 2023; Tran et al., 2025). Moreover, electrochemical (EC) sensors and field-effect transistor (FET)-based biosensors functionalized with antibodies or aptamers targeting specific surface markers have emerged as highly sensitive techniques for EVs quantification. EC sensors rely on redox-active reporters (Wang et al., 2017) or enzymatic reactions (alkaline phosphatase or horseradish peroxidase)(Jeong et al., 2016; Mathew et al., 2020) to amplify binding signals, thereby achieving high sensitivity in EV detection. FET-based biosensors exploit the transistor structure to transform bio-signals from EV binding to the sensing surface into measurable electrical signals (An et al., 2023; Ramadan et al., 2021). While EC and FET biosensors can be applied in the context of EV-based diagnostics, they are not ideal solutions for quality control applications required, for example, in EV-based drug-delivery. Indeed, the engineering steps involved in producing drug-delivery EVs can inherently modify the abundance and spatial organization of membrane proteins, rendering marker-dependent measurements unrepresentative of the total vesicle population (Hong and Ndukaife, 2023; Xu et al., 2025). To support robust, high-throughput quality control in manufacturing, monitoring strategies should ideally be pan-specific, capturing all vesicles irrespective of individual protein expression. Moreover, protein-based approaches require sophisticated equipment and technical expertise, limiting their applicability in this scenario.

In recent years, organic electrochemical transistors (OECTs) have gained significant attention in bioelectronics due to their unique ability to transduce biological signals into electronic outputs (Gkoupidenis et al., 2023; Granelli et al., 2025; Guo et al., 2024; Rivnay et al., 2018; Saleh et al., 2024; Salvigni et al., 2024). OECTs are three-terminal devices where the electronic conductivity of an organic mixed ionic-electronic material (OMIEC) channel connected to two electrodes, named source and drain, is modulated by a third electrode, named gate. The operation of OECTs relies on the interaction between ionic and electronic charges, facilitated by direct contact between the electrolyte and the transistor channel (Cea et al., 2023; Rashid et al., 2021; Romele et al., 2019). This results in a sub-nanometric ionic-electronic interaction that spans the entire microscale volume of the channel. The volumetric response generates substantial ionic-electronic transduction, leading to significant signal amplification, a key feature that enhances biosensing capabilities. Additionally, OECTs are compatible with aqueous environments and possess tunable chemical and structural properties, making them suitable for a wide range of bioelectronic applications across various fields, including for example high-density iontronic circuits (Huang et al., 2023; H. Kim et al., 2024; Koutsouras et al., 2023), bio-chemical sensors (Granelli et al., 2022; Lieberth et al., 2021; Romele et al., 2020), and neuromorphic biosensing systems (Belleri et al., 2024; Ji et al., 2025; Sarkar et al., 2022). Recent advancements have shown that OECTs can be employed for real-time, non-invasive monitoring of cells exposed to tumor-derived EVs (Lieberth et al., 2023; Traberg et al., 2023). The optically transparent channel of OECTs allowed simultaneous electrical and optical measurements, providing a robust platform for phenotypic screening. While these developments highlight the potential of OECT-based bioelectronics, OECT approaches for EV quantification remain largely unexplored. The chemical tunability of OECTs, combined with their ability to convert biological signals into highly amplified electronic responses, could serve as a critical advantage in developing systems for high-throughput, reliable EV quantification.

Therefore, despite the rapid expansion of extracellular vesicle (EV) research, robust and scalable methods for EV quantification in manufacturing and quality-control contexts remain limited. Particle-based techniques such as NTA provide size and concentration information but do not report on membrane protein presence or functional surface integrity. Conversely, antibody-based and FCM approaches are inherently marker-dependent and may undercount engineered or processed EVs when surface proteins are altered or partially shielded. Interestingly, recent high-throughput array-based strategies have addressed EV surface protein analysis using supramolecular probes or chemical capture platforms, enabling multiplexed and in situ characterization (Feng et al., 2025; X. Feng et al., 2023a, 2023b; Hu et al., 2025; Shen et al., 2024). In parallel, organic electrochemical transistors (OECTs) based on mixed ionic–electronic conductors have benefited from recent advances in materials design and operational stability (Chen et al., 2025; Feng et al., 2022; Wu et al., 2024; Yang et al., 2025), making them attractive for compact, electrically readable biosensing platforms.

Here we introduce a bioelectronic system enabling rapid, reliable, pan-specific and high-throughput EV quantification. Strain-promoted alkyne-azide cycloaddition (SPAAC) click chemistry mediates the covalent reaction between moieties immobilized on EV surface protein and OMIEC-functionalized channel, enabling pan-specific capture regardless of individual protein profile. The system compact design integrates a 3 $\times$ 4 matrix configuration of OMIEC-functionalized OECTs with 3D-printed fluidic devices housed in a disposable, low-cost cartridge operated by a silicon-based electronic reader, which provides automated operation, mixed-signal processing, and digital data communication. The proposed bioelectronic system detects membrane-protein-bearing EVs in less than 15 min, achieving a limit of identification as low as 6 $\times$ 10^6 particles per milliliter with a dynamic range spanning three orders of magnitude. By combining high sensitivity, throughput, and reliability with automation and user-friendly operation, the proposed approach addresses the gap between sophisticated laboratory techniques and practical implementation in scalable, automated workflows.

2. Experimental section

Materials: PEDOT:PSS (Clevios PH-500) was purchased from Heraeus Clevios GmbH and filtered with a 0.22 μm cellulose filter. Ethylene glycol (EG), (3-glycidyloxypropyl)trimethoxysilane (GOPS), Poly-L-lysine (PLL) solution, sodium azide (NaN_3), calcium ionophore (A23187) and phosphate-buffered saline (PBS) tablets were acquired from Sigma-Aldrich and were used without further purification. Sulfo-Cyanine5-DBCO was purchased from Lumiprobe GmbH. Dibenzocyclooctyne 4-Sulfo-2,3,5,6-tetrafluorophenyl (DBCO-STP) Ester, Azido-PEG4-NHS Ester were purchased from ClickChemistryTools. Silver/Silver Chloride ink (5874) was purchased from DuPont.

PEDOT:PSS:PLL–N_3 and PEDOT:PSS OECT fabrication: 100 nm thick Au source/drain/gate contacts are sputtered through a shadow mask on a glass substrate. An adhesion layer of 15 nm of Ti-W is previously deposited to enhance Au adhesion. Glass substrates are cleaned with DI water, dried with N_2, and reactivated by a UV-ozone treatment to promote PEDOT:PSS adhesion. PEDOT:PSS solution was spin coated (30 s, 2000 rpm) and mechanically patterned by using a wet cotton stick. The thickness of the PEDOT:PSS films is defined only by the spin coating conditions. The devices were annealed for 30 min at 140 °C. Arrays of twelve OECT channels were fabricated on the glass substrates with a channel width of 500 μm and a channel length of 70 μm. PEDOT:PSS is mixed with 5 vol% EG (to improve film conductivity) and 1 vol% GOPS (as a crosslinker). PEDOT:PSS:PLL–N_3 is obtained by adding to PEDOT:PSS a PLL solution (0.1 % w/v in H_2O) at a volume ratio of 75% v/v, based on a previously reported protocol.[38] Next, NHS-Peg_4-N_3 is added to the solution at a volume ratio of 0.5% v/v. The reaction is conducted overnight at 4 °C. The Ag/AgCl gate was printed by dispensing Ag/AgCl ink formulation with a G30 needle and baked at 120 °C for 2 min. Fabricated chip batches can be stored under dry conditions for at least one week prior to use.

3D printed fluidic device: Ad-hoc 3D-printed fluidics were designed to provide electrical access to the OECT matrix and a housing for the analyte during measurements. The fluidic structure defines four compartments, each aligned with one OECT array and the corresponding Ag/AgCl gate. The microfluidic device was fabricated with an O-ring seat patterned on its bottom surface, into which an elastomeric O-ring was placed and fixed using cyanoacrylate adhesive to form a gasket interface with the OECT substrate. Upon assembly, the gasket ensures physical contact and sealing between the fluidic compartment and the device surface, while aligning the fluidic openings with the active OECT areas and the Ag/AgCl gate.

AFM measurements: topography was investigated with AFM (Park NX10) in non-contact mode with a cantilever NSG30 by TipsNano. It is a High-Resolution Silicon AFM Cantilever with a tip radius around 6 nm operated at 256 kHz and an oscillation amplitude of 20 nm.

Fluorescence microscope: Fluorescence images of functionalized PEDOT:PSS:PLL–N_3 reacted with Sulfo-Cyanine5-DBCO were acquired by Syngene G:BOX Chemi XX9 with an acquisition time of 2 min and 640 nm wavelength.

Human blood collection and EV extraction: Red blood cells (RBCs) are obtained from anonymized healthy volunteers under written consent and provided by the A. O. Spedali Civili di Brescia, ethical approval "EritrEV NP5705". EVs were isolated following the guidelines from Usman et al. (2018) Briefly, after blood collection (100 mL), RBCs were pelleted by centrifugation at 1000×*g* for 8 min at 4 °C and washed three times in PBS without calcium and magnesium. RBCs were then washed two additional times with CPBS (PBS + 0.1 g/L calcium chloride) and transferred into a 75 mm^2 tissue culture flask. Calcium ionophore was added to the flask (final concentration 10 mM) and incubated overnight at 37 °C. RBCs (75 mL) were gently collected from the flask, and cellular debris was removed by differential centrifugation (600×*g* for 20 min, 1600×*g* for 15 min, 3260×*g* for 15 min, and 10,000×*g* for 30 min at 4 °C). The pellet was discarded at each step, transferring the supernatant into a fresh tube. The supernatants were filtered through 0.45 μm nylon syringe filters. EVs were collected by ultracentrifugation at 100,000×*g* for 70 min at 4 °C. EV pellets were then resuspended in cold PBS, layered above a 2 mL frozen 60% sucrose cushion, and centrifuged at 100,000×*g* for 16 h at 4 °C, with deceleration speed set to 0. The red layer of EVs was collected, washed twice with cold PBS, and spun at 100,000×*g* for 70 min at 4 °C. Finally, EVs were resuspended in 1 mL of cold PBS.

EVs functionalization with DBCO: EVs were functionalized following a one-step labeling strategy. 200 μL of 8 × 10^{11} EV ml^{-1} EV solution was reacted with 200 equivalents of DBCO-STP-ester (diluted in PBS) on continuous mixing. DBCO excess was removed using Vivaspin500 column with 10 kDa cut-off, washing the samples five times with 500 μL of PBS. DBCO-EVs were recovered from the column with 200 μL of PBS.

EVs control experiments: To generate control samples DBCO-EVs were treated as follows: after DBCO functionalization, EVs were reacted with 1000 equivalents of NaN_3 to inactivate every DBCO present on the EV surface and then purified as previously described. Another control sample was obtained by reacting EVs with 50 μg mL^{-1} trypsin for 6 h at 37 °C in order to cleave EV's membrane proteins. After this treatment EVs were purified by ultracentrifugation (100.000 g, 2 h) and then reacted with DBCO-STP-ester and purified as previously described.

Nanoparticle Tracking Analysis (NTA): NTA was performed according to the manufacturer's instructions using a NanoSight NS300 system conFig.d with a 532 nm laser. Samples were diluted 1:1000 in filtered PBS (0.22 μm) to a final volume of 1 mL to obtain the optimal particle per frame value (20–100 particles/frame). A syringe pump with constant flow injection was used (20 μl/min), and the temperature was set constant at 25 °C. Particles were detected at a camera level of 10 and three videos of 60 s were captured and analyzed with NTA software version 3.2. The mean, mode, and median EV sizes from each video were used to calculate sample concentration, expressed in particles ml^{-1}.

3. Results and discussion

3.1. OECT functionalization and stability

The core of the proposed platform is a disposable bioelectronic cartridge comprising channel-functionalized OECTs, integrated in a 3 × 4 matrix configuration. The structure of an OECT with lateral-integrated non-polarizable gate is illustrated in Fig. 1a. The main channel materials are highlighted. The functionalized ionic-electronic conducting channel is obtained by combining poly-L-lysine (PLL) with azide (N_3) moieties and poly (3,4-ethylenedioxythiophene)-poly (styrenesulfonate) (PEDOT:PSS). PLL, a positively charged polyelectrolyte, electrostatically interacts with the SO_3^- groups in PEDOT:PSS (Romele et al., 2019), allowing channel functionalization. Additionally, grafting PLL with N_3 moieties (PLL-N_3) introduces a functional component that enables the immobilization of biomolecules modified with dibenzocyclooctyl (DBCO) onto the OECT channel exploiting rapid, catalyst-free bioorthogonal click reactions. Specifically, the strain-promoted alkyne-azide cycloaddition (SPAAC) reaction results from the release of ring strain within a cyclic octyne (Bhatta et al., 2023; Di Iorio et al., 2022; Scinto et al., 2021). Therefore, we hypothesized that functionalizing EVs with DBCO, which selectively binds to amine groups on membrane proteins, would result in the covalent binding of EVs–DBCO to PEDOT:PSS:PLL–N_3 channels, eventually resulting in an electronic current dependent on the concentration of EVs in the sample assayed.

To test the feasibility of these concepts, we first investigated the binding efficiency by varying the concentration of functional groups. The density of functional groups plays a pivotal role in achieving uniform and consistent functionalization across the OECT channel and maximize the efficiency of bonding. We measured the fluorescence of PEDOT:PSS:PLL–N_3 films across various N_3/PEDOT:PSS:PLL percentage volume concentrations, using a DBCO-functionalized fluorophore (sulfocyanine5.5, Cy5.5). Each sample was incubated with DBCO–Cy5.5, followed by thorough washing with a solution of PBS and surfactants. Further details are reported in the Experimental Section. The overall

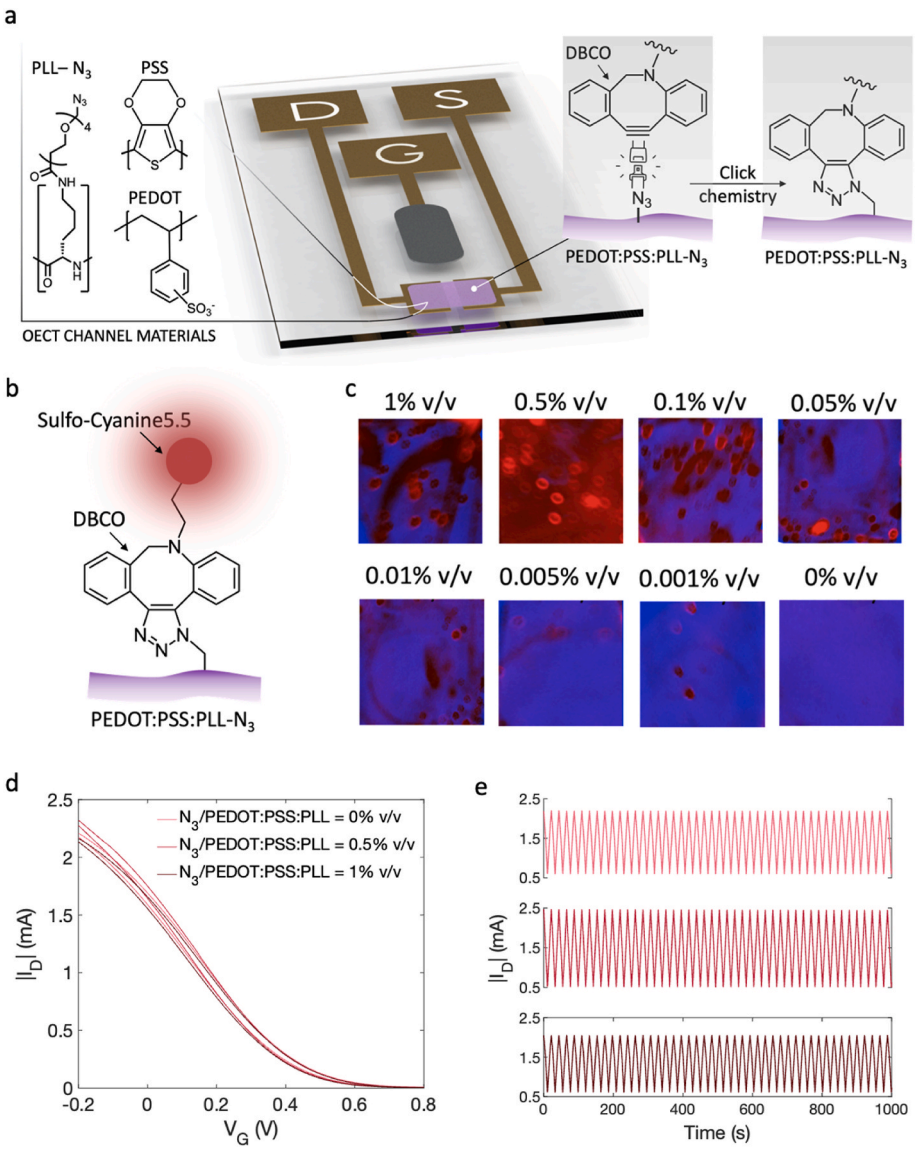

Fig. 1. Functionalized-channel OECTs. a) Schematic representation of the PEDOT:PSS: PLL–N_3 OECT channel with non-polarizable side-gate printed electrode. On the right, a focus on the OECT channel materials. On the left, click chemistry reaction of azide moieties in the channel and DBCO. b) Schematic illustration of PEDOT:PSS:PLL–N_3–DBCO–Cy5.5 upon click chemistry reaction. The fluorophore tags allow fluorescence microscopy analysis. c) Fluorescence microscopy images of PEDOT:PSS:PLL–N_3 films at several volume percentage N_3/PEDOT:PSS:PLL concentration. d) Measured double-sweep transfer characteristics (I_D-V_G) at $V_D = -0.1$ V of PEDOT:PSS:PLL–N_3 OECTs at various N_3/PEDOT:PSS:PLL volume ratio. e) Cycling stability of PEDOT:PSS: PLL–N_3 OECTs at various N_3/PEDOT:PSS:PLL volume ratio. $V_D = -0.1$ V, V_G is swept between −0.2 V and 0.3 V with a sweep rate of 50 mV s^{-1} 1 × PBS solution is used as electrolyte.

assay is depicted in Fig. 1b and the acquired fluorescence images as a function of N_3/PEDOT:PSS:PLL concentration are displayed in Fig. 1c. Azide density was optimized to balance surface reactivity and preservation of OECT electrochemical performance. The best result in terms of intensity and uniformity is obtained in the case of N_3/PEDOT:PSS:PLL = 0.5% v/v, while larger or smaller concentrations give a significantly reduced intensity. As a control experiment N_3/PEDOT:PSS:PLL = 0% v/v (no azide groups) exhibits a distinct dark area, demonstrating the specificity of the click-chemistry between N_3 and DBCO and the absence of nonspecific interactions between DBCO and PEDOT:PSS:PLL backbone.

To evaluate the impact of azide moieties in the channel on OECT performance, we fabricated PEDOT:PSS:PLL–N_3 OECTs with N_3/PEDOT:PSS:PLL ratios of 0%, 0.5%, and 1% v/v, each with nominally identical geometries. In all cases PBS solution is used as electrolyte. The measured transfer characteristics are displayed in Fig. 1d and Fig. S1. By applying a positive gate voltage (V_G) cations drift into the polymer, reduce the hole concentration and lower the drain current (I_D). Analogously, when a negative V_G is applied previously injected cations drift out of the polymer while anions drift into the polymer, the hole concentration increases, and this results in a larger I_D. The almost perfectly aligned $I_D - V_G$ curves observed across the various formulations of PEDOT:PSS:PLL–N_3 OECTs demonstrate the safeguarding of device functionality by the functionalization protocol, regardless of the N_3/PEDOT:PSS:PLL volume ratios. As a further confirmation, the transconductance and gate current as a function of gate voltage is displayed in Fig. S2 and Fig. S3, respectively. The maximum transconductance is larger than 4 mS at $V_G = 0.1$ V and $V_D = -0.1$ V, in full agreement with state-of-art OECTs (Frusconi et al., 2024a, 2024b). Importantly, transfer characteristics and transconductance remained nearly unchanged across 0%, 0.5% and 1% v/v N_3 formulations, demonstrating that the grafting protocol preserves mixed ionic–electronic transport while enabling efficient surface functionalization. Fig. 1e shows highly stable cycling behavior across all devices, with no variation in drain current observed over 1000 s of

cycling tests. The cycling protocol was designed to reflect the electrochemical operating regime of the platform during sensing measurements, thereby providing an assessment of device stability. Key electrical parameters (i.e., maximum and minimum drain current and maximum transconductance) were monitored during continuous operation for up to 6000 s, as reported in Fig. S4. These results indicate that functionalized PEDOT:PSS:PLL–N_3 OECTs provide stable current modulation and large transconductance, making them an ideal platform for biomolecule immobilization and reliable quantification.

3.2. Bioelectronic system

Rapid, reliable, and high-throughput EV quantification require the design of a platform capable of conducting multiple and repeated assays concurrently, including control experiments for real-time data validation. A schematical overview of the proposed bioelectronic system is shown in Fig. 2. We integrated PEDOT:PSS:PLL–N_3 OECTs in a four-arrays configuration, as depicted in Fig. 2a. Each array is made of three OECT channels with a common non-polarizable side-gate printed

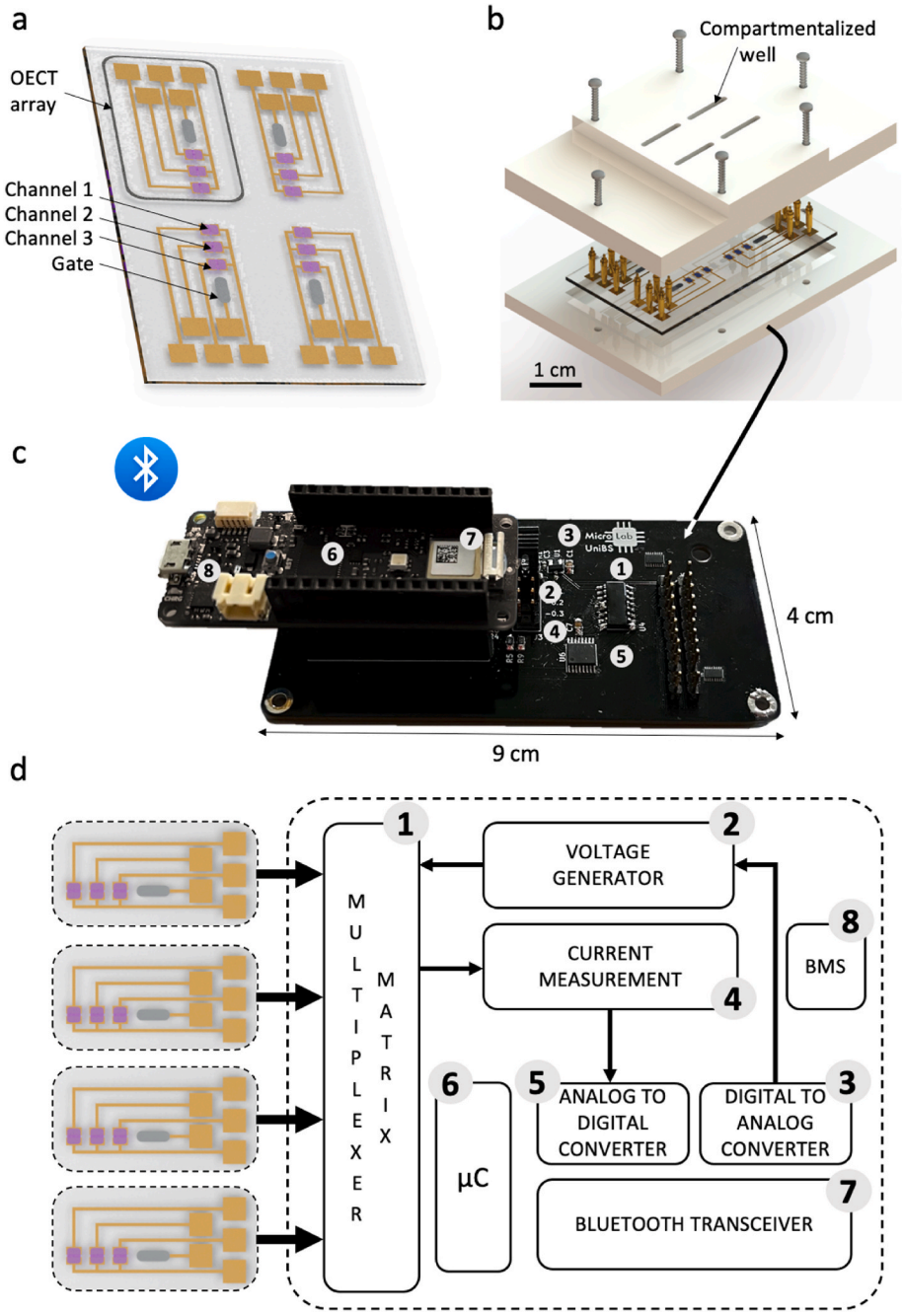

Fig. 2. Bioelectronic system. a) Schematic illustration of the bioelectronic sensing matrix with 4 arrays of OECTs. Each array comprises 3 OECT channels and a printed Ag/AgCl gate electrode. b) Disposable bioelectronic cartridge obtained assembling the sensing matrix with a 3D printed fluidic device. Each OECT array has a compartmentalized well, allowing four analyses in parallel. c) Silicon-based electronic reader designed with a very compact form factor (9 cm × 4 cm) allowing the automatic operation of the bioelectronic cartridge and the Bluetooth connection with a smart device for data transfer and visualizations. d) The main building blocks of the bioelectronic system are displayed. The bioelectronic cartridge is electrically connected to the reader. Each array is addressed by means of a multiplexer matrix (block 1). The main blocks of the reader include the voltage generator (2), the digital-to-analogue converter (3), the current measurement unit (4), the analogue to digital converters (5), the microcontroller (6), the Bluetooth transceiver (7), and the battery management system (8). (For interpretation of the references to colour in this figure legend, the reader is referred to the Web version of this article.)

electrode. The 3 × 4 OECT matrix is combined with a 3D printed fluidic device (Fig. 2b and Fig. S5). The 3D fluidic device comprises four compartments and allows a reliable electrical connection with the OECT matrix. Each fluidic compartment contains an OECT array, ensuring that each trio of OECTs can be exposed to a different sample. Therefore, this disposable bioelectronic cartridge allows the parallel analysis of four different samples and, for each of them, three replicates are obtained at the same time. The bioelectronic cartridge is connected to an ultra-portable and reusable silicon-based electronic reader, displayed in Fig. 2c. The reader operates the cartridge by generating and measuring all the signals and allows the connection with a smart device (e.g. phone, tablet, computer). The main building blocks of the electronic reader are shown in Fig. 2d. An array of transistors is selected by the multiplexer matrix (block 1, Fig. 2d). The operational procedure involves the acquisition of drain current I_D for the various OECTs within each compartmentalized well. The source electrodes are grounded throughout the characterization, thus operating in common source configuration. More in detail, during each step, the switch matrix selects the gate terminal to apply V_G and the drain terminals to apply V_D, and measure the corresponding drain current I_D. The gate voltage is generated by a voltage generator (block 2) connected to a digital-to-analogue converter (DAC, block 3). The DAC allows conversion of a digital code in an analogue signal, which is applied to the gate as a function of time. The drain current of the three OECTs in the array are measured by the read-out circuits based on multi-scale transimpedance amplifiers (block 4). The analog signals are converted into digital data (block 5), recorded by the microcontroller unit (block 6), and transmitted by Bluetooth (block 7) to a smart device. A battery pack powers the reader, with the battery management system (BMS, block 8) monitoring the battery status and managing the charging. The integrated system automatically performs

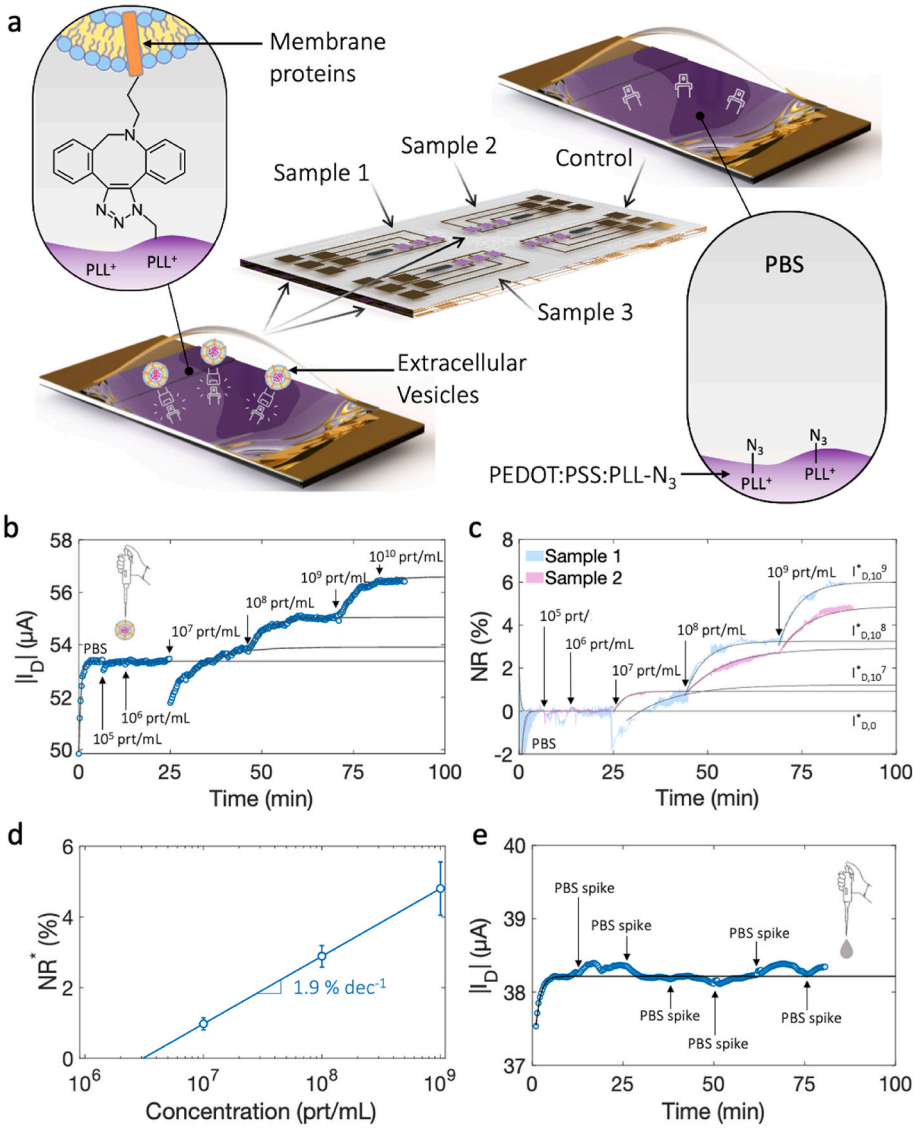

Fig. 3. Real-time quantification of EVs. a) Visual representation of the assays performed using the bioelectronic matrix. Array 1, 2, and 3, are exposed to samples 1, 2, and 3, respectively, each collected from a different subject. Array 4 is used for control experiments with PBS (reference fluid). b) Real-time drain current ($V_G = 0.3$ V and $V_D = -0.1$ V) measured from an OECT of array 1 as a function of EV concentration. Black lines are guide for the eye. c) Real-time normalized response (NR) as a function of EV concentration. The light blue and purple areas (Sample 1 and 2) represent the spread of measured data for the three channels within the same array, with black lines as guide for the eye. d) Calibration curve obtained from assays performed with array 1-3. $NR^* = 100 \times (I^*_D\text{-}I^*_{D0})/I^*_{D0}$, where I^*_D is the steady-state current at any given EV concentration, and I^*_{D0} is the steady-state current measured with only PBS (baseline). Symbols represent the average, and bars indicate the standard deviation calculated from nine replicates. The line is the least square linear approximation of the measurements. e) Real-time monitoring of drain current ($V_G = 0.3$ V and $V_D = -0.1$ V) during consecutive PBS spikes into the array 4, showing excellent stability of the bioelectronic system. (For interpretation of the references to colour in this figure legend, the reader is referred to the Web version of this article.)

the various measurements, and the user has only to dispense the fluids into the wells of the disposable cartridge, making it an ideal solution for seamless in-line quality control with minimal user intervention, thereby reducing operator-dependent variability.

3.3. EV pan-specific quantification

To systematically study the quantification of membrane-protein-bearing EVs by means of the proposed bioelectronic system, we isolated EVs from RBC extracted from peripheral blood samples of three healthy donors. Then, we functionalized EVs with DBCO, which selectively binds to amine groups on membrane proteins, and the EV concentration of the original sample amounts to 10^{12} particle ml^{-1}. Quantitative analysis of DBCO functionalization across independently labeled EV batches confirms reproducible labeling (Fig. S6 in the Supplementary Data). Physicochemical characterization before and after DBCO functionalization shows no significant changes in EV size distribution or surface charge, suggesting preserved vesicle integrity and stability (Table S1 in the Supplementary Data). Details on samples collection and quantification procedures are given in the Experimental Section. It is worth noting that RBC-derived EVs were selected as a highly relevant and scalable reference system for manufacturing-oriented workflows. Therefore, the proposed sensing strategy does not rely on a specific EV marker but targets generic primary amines on membrane proteins through click chemistry. As such, the approach is potentially transferable to EVs derived from different cell sources provided that accessible surface proteins are present. The bioelectronic cartridge for sample analysis is organized as displayed in Fig. 3a. Three functionalized OECT arrays are used for the quantification of EVs collected from three different subjects, and one array is used for control experiments. Specifically, sample in array 1 is used for EV quantification at various concentrations, in order to obtain the calibration curve. To mimic conditions relevant for therapeutic applications, as a first step the corresponding well is filled with 400 μL PBS, which is the liquid used for EVs dispersion. The drain currents of the OECTs in array 1 are recorded as a function of time. Measurements are performed under constant bias conditions in a high-ionic-strength electrolyte, ensuring stable device operation and consistent electrochemical gating. A volume of 100 μL of sample 1 is spiked into the well, to obtain an initial concentration of 10^5 particle ml^{-1}. Then, EV concentration is incrementally increased in steps of 10, from 10^5 to 10^{10} particle ml^{-1}, and the measured OECT currents mirror the covalent binding dynamic.

Fig. 3b shows the recorded I_D (symbols) as a function of EV concentration from an OECT of the array 1. In PBS alone (without EVs), after an initial transient response I_D stabilizes to a steady-state value $I^*_{D0} = 53.5\ 10^{-6}$ A. When the EV concentration is 10^5 particle ml^{-1}, the recorded I_D aligns with I^*_{D0}, showing negligible variation of the steady-state value. Increasing the EV concentration to 10^6 particle ml^{-1}, an analogous behavior is observed. When the EV concentration is 10^7 particle ml^{-1}, an initial current reduction with transient recovery is displayed, and then a plateau is obtained. Importantly, the steady-state current recorded at an EV concentration of 10^7 particle ml^{-1} is larger than that measured at 10^6 particle ml^{-1}. This is further confirmed by further increasing the EV concentration to 10^8 and 10^9 particle ml^{-1}. The increase in drain current observed upon EV binding can be rationalized considering OECT operation in depletion mode. More in detail, the OECT drain current is determined by the equilibrium doping level of the channel, which depends on the electrochemical coupling (Romele et al., 2019). Covalent immobilization of EVs modifies the channel–electrolyte interface by introducing a hydrated, dielectric and ion-accessible layer that alters the effective capacitive coupling and the distribution of the applied gate potential. As a consequence, for a given gate voltage, a smaller fraction of the applied potential effectively contributes to volumetric dedoping of the PEDOT:PSS channel. This results in a higher equilibrium doping level and therefore a higher steady-state drain current. The larger response observed when click chemistry is enabled, together with AFM evidence of increased surface coverage, supports this interpretation.

To corroborate the results, the same assay was performed in another array (array 2) using another sample (sample 2). To directly compare the various experiments performed with different OECT arrays, we defined the normalized response $NR = 100 \times (I_D\text{-}I^*_{D0})/I^*_{D0}$, as the relative variation of the drain current I_D with respect to the baseline I^*_{D0}. Each well integrates three OECT channels that act as parallel replicates; normalization of the drain current to the baseline value mitigates minor geometric variations, resulting in consistent responses across channels. Fig. 3c shows NR over time as EV concentration is varied from 0 (PBS only) to 10^9 particle ml^{-1} from sample 1 (light blue area) and sample 2 (purple area), with three replicates for each. The two samples, collected from different donors, are assayed with two different OECT arrays, and consistent bioelectronic responses are obtained. The very good agreement between the various results suggests that once the calibration curve is obtained, it can be used for multiple experiments and does not need to be reacquired each time an assay is performed.

Fig. 3d depicts the calibration curve obtained as the steady state normalized response $NR^* = 100 \times (I^*_D\text{-}I^*_{D0})/I^*_{D0}$, where I^*_D is the steady-state current at any given EV concentration. NR* logarithmically increases with the EV concentration, and the least squares linear approximation (blue line in Fig. 3d) shows a sensitivity of 1.9 % dec^{-1}. Calibration curves were derived from nine independent measurements (three channels across three arrays). Intra-array and inter-array repeatability were quantified by calculating the coefficient of variation (CV%) of steady-state normalized responses (NR*), as summarized in Table S2 and Fig. S7. While the proposed approach relies on reproducible pre-labeling of EV membrane proteins (Fig. S6), absolute labeling efficiency is not required for quantification, as the assay is calibrated through the device response and primarily depends on consistency of functionalization across batches. As a control experiment, another OECT array of the bioelectronic cartridge is operated in the same conditions by spiking PBS without EVs. The current as a function of time measured while adding multiple-times 100 μL of PBS (reference fluid) is displayed in Fig. 3e. After an initial transient dynamic analogous to the experiments discussed above, the drain current is independent of the PBS spikes, showing an excellent stability of the bioelectronic platform. We note that the bioelectronic system performed all measurements in parallel, providing two independent and consistent calibration curves (sample 1 and sample 2), the quantification of sample 3, and control experiments, each in triplicate.

3.4. Impact of click chemistry

As a next step, we quantitatively investigated the impact of click chemistry on the sensing performance. Fig. 4a represents the bioelectronic matrix setup. Arrays 1, 2, and 3 comprise OECTs with PEDOT:PSS:PLL-N_3 channel. Array 1 is exposed to EVs functionalized with DBCO, array 2 is exposed to EVs without DBCO, and array 3 is exposed only to PBS. Fig. S8 shows the raw measurements of bioelectronic cartridge arrays. Fig. 4b shows NR over time as a function of EVs concentration. The data points are the average values over three replicates taken from the three OECTs in array 1. NR remains unaffected upon exposure of functionalized OECTs to EV concentrations 10^5 and 10^6 particles ml^{-1} while at larger concentrations a consistent increase is displayed. These results are in full agreement with the previous ones and confirm EV quantification as well as proper and successful execution of the assay. To evaluate the role of click-chemistry on the sensing response, OECTs in array 2 are exposed to EVs without DBCO, thus excluding the click chemistry reaction with the PEDOT:PSS:PLL-N_3 functionalized channels. Analogous to the procedure conducted in array 1, measurements began with PBS alone. After the current stabilized at a steady-state value, the EV concentration was incrementally increased from 10^5 to 10^{10} particle ml^{-1} in steps of a factor 10. The normalized response measured from array 2 OECTs exposed to EVs without DBCO is

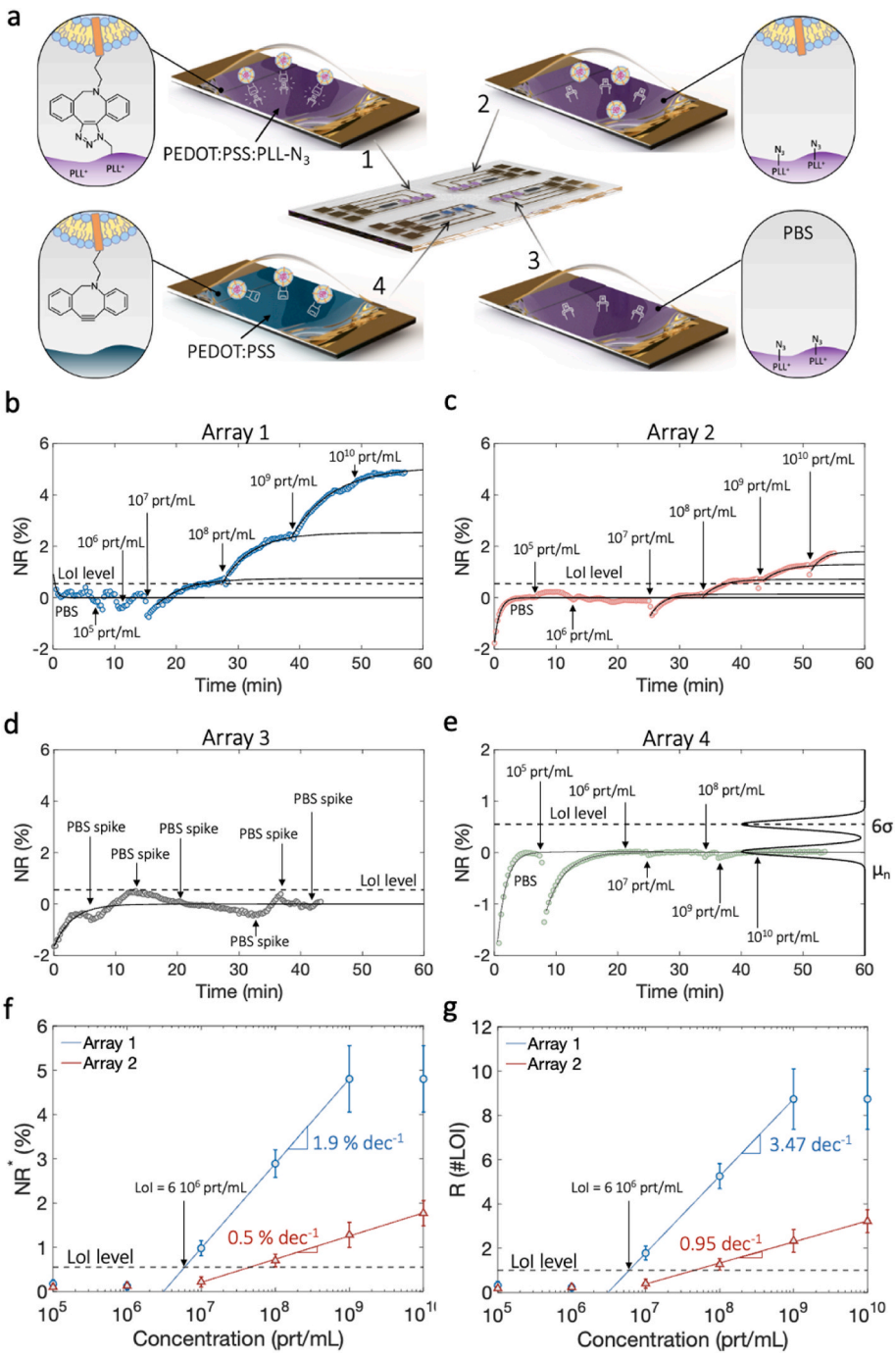

Fig. 4. Reliable EV quantification. a) Visual representation of the assays performed using the bioelectronic matrix. Array 1, 2, and 3, are PEDOT:PSS:PLL–N_3 OECTs. EVs functionalized with DBCO are assayed in array 1. EVs without DBCO are assayed in array 2. Array 3 is used as control experiment. In array 4 EVs functionalized with DBCO are assayed with non-functionalized PEDOT:PSS OECTs. b) Measured real-time normalized response (NR, symbols) as a function of EV-DBCO concentration obtained from PEDOT:PSS:PLL–N_3 OECTs in array 1. Black lines are guide for the eye. c) Real-time NR as a function of EV concentration obtained from PEDOT:PSS:PLL–N_3 OECTs in array 2. d) Control experiment with array 3 exposed to various spikes of PBS. e) Real-time NR as a function of EV-DBCO concentration obtained from PEDOT:PSS OECTs in array 4 (negative control experiment). On the right axis, the Gaussian distribution of the measured random error is displayed. The LoI is calculated as the average of the measured noise level ($\mu_n = 0$) plus 6 times its standard deviation, σ. In panels b-g, the LoI level calculated from the measurements in panel e is shown in dashed line. f) Calibration curve and g) Sensing response R = NR*/LoI vs EV concentration obtained from assays performed with array 1 (blue circle, click chemistry) and array 2 (red triangle, without click chemistry), respectively. Symbols are the mean value and bars indicate the standard deviation calculated from three replicates. The lines represent the least square linear approximation. (For interpretation of the references to colour in this figure legend, the reader is referred to the Web version of this article.)

displayed in Fig. 4c. NR is independent of the EV concentration up to 10^7 particle ml^{-1}. A change in the response is measured when the EV concentration is 10^8 particle ml^{-1} and NR consistently increases by increasing the concentration in the range 10^8 to 10^{10} particle ml^{-1}. This residual response could be attributed to physisorption of EVs on the functionalized channels, mainly due to the PLL-enhanced electrostatic interactions with negatively charged biomolecules under physiological conditions (Ridolfi et al., 2020). Interestingly, comparing the

normalized responses obtained when assaying EVs with and without DBCO (Fig. 4b and c), results that without click-chemistry the maximum NR is about three times smaller than that observed when click-chemistry is involved. This behavior is consistent with reproducible DBCO-mediated EV functionalization and with effective functionalization of the PEDOT:PSS:PLL channel with the corresponding reactive moieties. Therefore, when DBCO-EVs are introduced, devices with N_3 group densities other than 0.5% show a reduced, non–steady-state NR response (Fig. S9 in the Supplementary Data). In parallel with assay 1 (EVs with DBCO) and assay 2 (EVs without DBCO), the channel-functionalized OECTs in array 3 were exposed to various spikes of PBS. As shown in Fig. 4d, the measured NR remained unaffected by the PBS spikes. This control experiment confirms the excellent stability of the bioelectronic system.

3.5. Reliability of the bioelectronic system

To assess the reliability of the bioelectronic system, we used the array 4 of the cartridge to obtain the limit of identification (LoI), that assures a level of confidence larger than 99 % and, differently from the limit of detection (LoD), both false positives and false negatives are lower than 1%. We fabricated an array of three OECTs with PEDOT:PSS channel (viz. without functionalization) and we measured NR when exposed to EV concentration in the range 10^5 – 10^{10} particle ml^{-1}. Fig. 4e shows the average NR as a function of time over three replicates measured in parallel and exposed to the very same liquid sample. The measurements start with PBS solution and after an initial transient dynamic, a steady-state value is achieved. Spiking EVs to obtain a final EV concentration of 10^5 particle ml^{-1}, I_D instantaneously decreases and then increases reaching the same value recorded before the addition of EVs (viz. with only PBS). A subsequent increase of EV concentration from 10^6 to 10^{10} particle ml^{-1} does not result in any variation of the recorded current. These results prove that in the absence of N_3 and PLL used for channel functionalization, no significant difference is recorded between the baseline current (PBS only) and sensing signal upon EV exposure. The random error Gaussian distribution is featured in Fig. 4e (right axis), around the mean value μ_n. We calculate the LoI as the average of the negative control experiment noise level ($\mu_n = 0$) plus 6 times its standard deviation, σ. The Gaussian distribution of the random error at the LoI is also displayed in Fig. 4e (Gaussian distribution with mean value of 6σ). The black dashed lines in Fig. 4b–d serve as visual representations of the LoI level.

To qualitatively investigate the interaction between EVs and the OECT channels with and without functionalization, we performed AFM measurements to examine the EV coverage on the channel surface. The acquired topographic images are displayed in Fig. S10. As a first step, we measured EVs physiosorbed on glass slides as a reference (Fig. S10a), finding EVs with dimension and shape in full agreement with state-of-art (Ridolfi et al., 2020). Then, EVs on PEDOT:PSS and PEDOT:PSS:PLL–N_3, used as channel of non-functionalized and functionalized OECTs, respectively, are shown in Fig. S10b and S10c. EVs on the PEDOT:PSS film are clearly observable, indicating a relatively weak interaction, akin to EVs physiosorbed on glass. In contrast, in the case of PEDOT:PSS:PLL–N_3 channel the EVs are covering a substantial area of the polymer, suggesting a more robust and stable bonding. Fig. 4f compares the calibration curves obtained with (blue circles) and without (red triangles) click chemistry. The comparison with the LoI level (dashed black line) shows that a LoI equal to 6×10^6 particle ml^{-1} and 5×10^7 particle ml^{-1} is obtained with (array 1) and without (array 2) click chemistry, respectively, confirming that click chemistry provides superior performance in terms of reliability and sensitivity. Moreover, to directly quantify the reliability of the assay, we defined the sensing response (R) with respect to the LoI level: $R = NR^*/LoI$. Fig. 4g shows R as a function of EV concentration. In array 1 we found $R = 1$ when EV concentration is 6×10^6 particle ml^{-1} and it increases up to $R = 8.8$ at an EV concentration of 10^9 particle ml^{-1}. In array 2 a maximum $R = 3.4$ is achieved only when the EV concentration is equal to 10^{10} particle ml^{-1}. Therefore, combining electrostatic interaction with click chemistry reduces the LoI by more than one order of magnitude with about a three-fold increasing of the sensitivity.

3.6. Pan-specific quantification of EVs using SPAAC-OECTs

Finally, we analyze the specificity of the interaction between EVs and PEDOT:PSS:PLL–N_3 channels considering EVs with DBCO-functionalized membrane proteins, EVs functionalized with neutralized DBCO, and EVs without membrane proteins. As displayed in Fig. 5a, array 1 of the bioelectronic cartridge is exposed to EVs functionalized with DBCO following the protocol described in the previous section. The recorded NR as a function of EV concentration is shown in Fig. 5b and confirms the previously observed outcomes, providing feedback on the proper and successful operation of the assay. In array 2 (Fig. 5c) PEDOT:PSS:PLL–N_3 channel is exposed to EVs functionalized with neutralized DBCO. To neutralize the DBCO moieties grafted onto the EVs' membrane proteins, we treated them to interact with complementary click chemistry moieties (further details are provided in the Experimental Section). As displayed in Fig. 5d, EV concentrations up to 10^7 particle ml^{-1} do not affect the NR. Increasing the EVs concentration from 10^7 to 10^8 particle ml^{-1} causes a shift in the measured OECT current and NR rises consistently within the range 10^8 to 10^9 particle ml^{-1}. The recorded response is comparable to that obtained when EVs without DBCO were assayed (see Fig. 4c) and can be attributed to the physisorption of EVs on the OECT channel, indicating that active DBCO handles are required to produce the enhanced bioelectronic response. Then, array 3 of the bioelectronic matrix is exposed to increasing concentration of EVs without membrane protein (Fig. 5e). To validate the selective binding of DBCO to the amine groups of the membrane proteins, the DBCO functionalization procedure was applied also to EVs without membrane proteins. Fig. 5f shows that when spiking EVs in the range 10^5 to 10^9 particle ml^{-1} the measured NR is below the LoI level and up to a concentration of 10^8 particle ml^{-1} is almost equal to the baseline obtained with PBS only. The lack of signal across the tested concentration range supports the requirement of functional membrane proteins for DBCO-mediated EV binding. Accordingly, the bioelectronic system quantifies EVs bearing membrane proteins and it is not sensitive to EVs without membrane proteins, as in this case NR is below the LoI level (Fig. 5f). As a last control experiment, PEDOT:PSS:PLL–N_3 OECTs of array 4 undergo consecutive spikes of PBS (Fig. 5g) and the recorded NR shown in Fig. 5h is in all cases below the LoI level, validating the excellent stability of the system. The raw data measurements of the various arrays are displayed in Fig. S11. As a comparison between the various experiments, Fig. 5i shows R as a function of EV concentration obtained from the various arrays. Array 1 (blue circles) is in full agreement with the measurements described in the previous section (see for example Fig. 4g) and the least squares linear approximation of the measured sensing response provides a LoI = 6.2×10^6 particle ml^{-1}. In array 2 (red triangles) EVs are functionalized with neutralized DBCO and therefore click-chemistry does not play a role providing a LoI = 2.5×10^7 particle ml^{-1}, which is about one order of magnitude larger than the LoI obtained with click chemistry. Moreover, the reduced sensitivity of NR results in a four-fold decrease of the maximum R. In the case of array 3 (green squares) the functionalized OECTs were exposed to EVs without membrane proteins and the response is below the LoI level ($R < 1$) in the whole range of EV concentration, underscoring that EVs without membrane proteins are not detected by the bioelectronic system.

3.7. Benchmarking

To understand the distinctive performance and positioning of our approach, we benchmarked the proposed bioelectronic system against established EV quantification methods. The performances are summarized in Table 1. Note that the proposed system operates on an

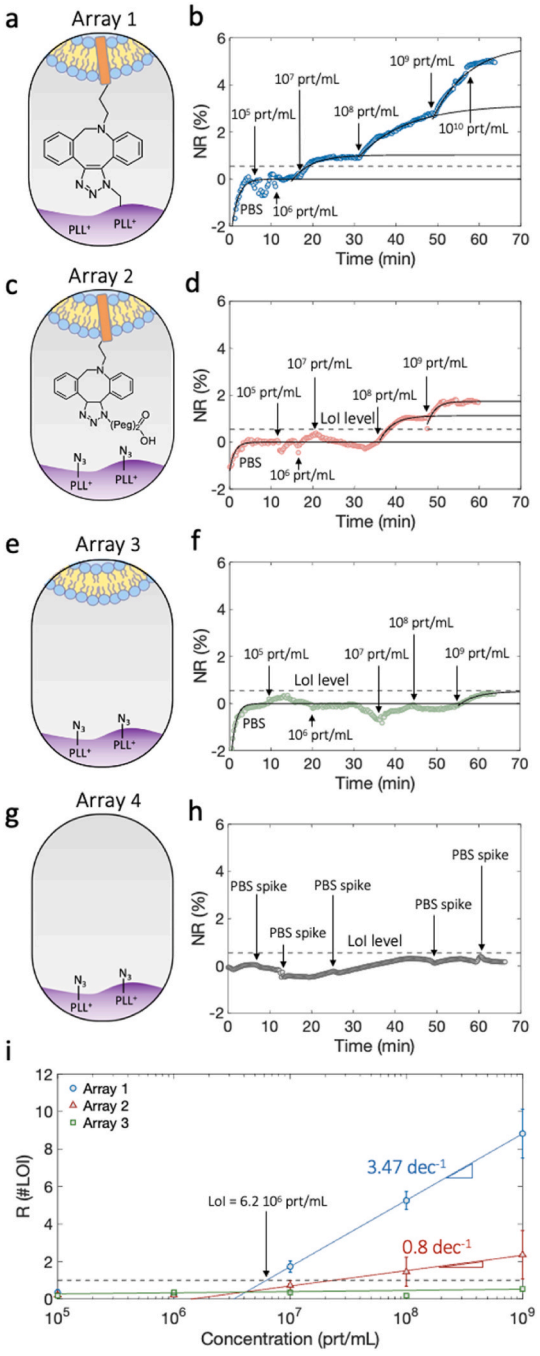

Fig. 5. Specificity of EV quantification. a) EVs functionalized with DBCO assayed with array 1. b) Real-time NR as a function of DBCO-functionalized EV concentration. c) EVs functionalized with neutralized DBCO assayed with array 2. d) Real-time NR as a function of EVs with neutralized DBCO. e) EVs without membrane proteins assayed in array 3. f) Real-time NR as a function of EVs without membrane proteins. g) Array 4 is used as Control experiments with PBS performed in array 4. h) NR measured when OECTs in array 4 are exposed to various spikes of PBS. In panels b,d,f,h), the LoI level is shown with dashed line and black lines are guide for the eye. i) Sensing response R as a function of EV concentration obtained from assays performed with array 1 (blue circle, click chemistry), array 2 (red triangle, without click chemistry), and array 3 (green squares, without membrane proteins). Symbols are the mean value, and bars indicate the standard deviation calculated from three replicates. The lines represent the least square linear approximation. (For interpretation of the references to colour in this figure legend, the reader is referred to the Web version of this article.)

inherently different principle: while NTA reports only particle counts and FCM, EC, and FET rely on specific surface markers that are not universally expressed due to EV heterogeneity, our OECT-based system quantifies vesicles through click-chemistry-driven covalent coupling between membrane proteins and functionalized transistor channels, enabling direct, marker-independent, and pan-specific assessment of total vesicle abundance in native buffer conditions. The comparison highlights that our pan-specific platform can deliver rapid, comprehensive information suitable for high-throughput monitoring in EV manufacturing pipelines. Specifically, high throughput quality control demands minimized analysis time and parallel multiple-sample processing. For example, NTA requires ~30 min per assay due to sequential particle tracking and extensive data acquisition, limiting throughput and necessitating multiple instruments for parallel processing, which increases cost and complexity. In addition, NTA measurements are sensitive to particle concentration, refractive index, and operator-defined acquisition parameters, frequently requiring repeated dilutions and manual optimization to ensure reliable readout, which increases analysis time and inter-laboratory variability (Comfort et al., 2021). Multi-step protocols involving fluorescent labeling, washing, antibody incubation, and signal processing render traditional protein-based methods (e.g., FCM) challenging for in-line quality control applications. These approaches typically require high-end instrumentation, optical calibration, and frequent quality control procedures to maintain sensitivity, limiting portability and increasing operational costs in manufacturing environments (Welsh et al., 2020; Wu et al., 2023).

Likewise, the time-to-results in EC and FET-based approaches is often constrained by the ~30-45 min incubation required for EVs to diffuse and achieve equilibrium binding with surface-immobilized antibodies or aptamers through non-covalent interactions (e.g., hydrogen bonds, van der Waals, electrostatic forces). Ramadan et al. reported a 15-min incubation time by modifying the flat graphene FET channel surface with spherical carbon dots, increasing the capture rate through geometrical effects (Ramadan et al., 2021). Implementation of parallel measurement strategies allows these platforms to deliver multiple results concurrently, offering a key operational advantage. Nevertheless, EC assays require additional reagents and reaction steps, increasing assay complexity and impacting reproducibility (Jeong et al., 2016; Yin et al., 2023). FET devices can be affected by Debye screening that restricts the effective sensing range to ~1 nm under physiological ionic conditions (100–150 mM). Adjusting buffer ionic strength (e.g., 0.001X PBS) can improve sensitivity but necessitates multiple washing steps, which extends the assay time (Kwong Hong Tsang et al., 2019; Yin et al., 2023).

Owing to click chemistry EVs immobilization and OECT-based approach, our system performs three repeated analyses on four samples, delivering 12 independent results simultaneously in less than 15 min. One-step DBCO labeling of EVs with parallel sensor readout enables rapid and irreversible covalent immobilization, eliminating multiple incubations, sequential reagents, and washing steps. Real-time operation of the integrated bioelectronic platform is combined with high reliability, as evidence by the LoI calculated from specificity controls measured on non-functionalized OECTs (i.e., without PLL–N3) exposed to DBCO-EVs samples (see Section 2.5 and Fig. S12). Under the assumption of Gaussian noise, the LoI definition bounds random false-positives and false-negatives below 1%. We note that state-of-the-art EC and FET-based methods define the LoD as three times the signal-to-noise ratio, calculated from the distance between the blank signal (e.g. PBS) and instrumental noise. However, this approach does not account for biological interferents, non-specific binding, or other endogenous substances, which can contribute to false-positive signals and limit the biological relevance of the reported LoD (Gegenschatz et al., 2022). Moreover, LoD values are associated with a high rate of false negatives (~50%). Notably, these methods reach LoD as low as 10^4 particles ml^{-1}, capturing rare EV subpopulations relevant for early diagnostics. To fairly compare the sensing performance with our bioelectronic system,

Table 1
Performance of state-of-the-art EVs quantification methods. The Fig.s of merit include the EV marker detected, time-to-results, the number of simultaneous independent analysis performed (N), real time response (RT), integration, range of concentration, limit of detection (LoD[b]), and limit of identification (LoI[c]).

Technology	EV marker	Time to results (min.)	N	RT	Integration	Range (prt/ml)	LoD[b] (prt/ml)	LoI[c] (prt/ml)	Ref
NTA	No	30	1	×	✓	$10^7 \div 10^9$	10^7	N.A.	Comfort et al. (2021)
FCM	EV-specific protein markers	60-240	1	✓	×	$10^6 \div 10^9$	10^6	N.A.	Welsh et al. (2020)
FET	CD63	>30	1	×	✓	$5\ 10^6 \div 5\ 10^8$	$5\ 10^6$	$5\ 10^7$[a]	Kwong Hong Tsang et al. (2019)
FET	CD63	>15	1	✓	×	$10^4 \div 10^8$	10^4	$5\ 10^6$[a]	Ramadan et al. (2021)
FET	CD9	>15	1	×	×	$10^9 \div 10^{15}$	$6\ 10^9$	N.A.	An et al. (2023)
FET	GPC-1	45	6	×	✓	$10^6 \div 10^{10}$	10^6	N.A.	Yin et al. (2023)
EC	LZH8	>30	1	×	✓	$2\ 10^4 \div 10^{12}$	$2.1\ 10^4$	$7.8\ 10^9$[a]	Wang et al. (2017)
EC	CD63	60	4	×	✓	$3\ 10^6 \div 10^9$	$3\ 10^6$	N.A.	Jeong et al. (2016)
EC	EpCAM	210	1	×	×	$10^4 \div 10^9$	10^4	N.A.	Mathew et al. (2020)
OECT	Membrane proteins (click-chem)	15	12	✓	✓	$5\ 10^6 \div 10^9$	-	$5\ 10^6$	This work

[a] Calculated from the study findings; N.A.:data not available due to the absence of negative control experiments in the studies.
[b] The LoD was calculated by blank signal (PBS) plus three times its standard deviation of the blank.
[c] The LoI was calculated by negative control signal (no EV probes or interfering species) plus six times its standard deviation.

we calculated the LoI from specificity control measurements for state-of-the-art EC and FET-based methods. Our system LoI aligns with the best state-of-the-art methods, while offering rapid, high-throughput, pan-specific monitoring suited to EV production pipelines.

4. Conclusion

In this study, we present a pan-specific bioelectronic system for rapid, high-throughput quantification of EVs with membrane proteins, specifically designed to meet the practical demands of quality control in large-scale EV manufacturing pipelines. The platform integrates channel-functionalized arrays of OECTs into a 3 × 4 matrix configuration within a low-cost, disposable cartridge, enabling simultaneous analysis of multiple samples with minimal handling. This cartridge is operated by a custom-designed electronic reader that seamlessly communicates data with smart devices. By leveraging click chemistry, complementary reactive groups on EVs and OECT channels facilitate covalent, pan-specific capture, ensuring accurate quantification of bulk vesicle abundance and integrity, independent of individual surface protein expression. The system achieves a LoI as low as 6×10^6 particles ml^{-1} (1×10^{-15} M) across a dynamic range spanning three orders of magnitude, while eliminating washing steps and sequential reagent additions, thereby enabling rapid, automated, and reproducible operation. EVs derived from sources other than RBCs (e.g., EVs isolated from different cell types, milk, plant-derived vesicles, or biofluids such as plasma, serum, and urine)(J. Feng et al., 2023; Feng et al., 2025; X. Feng et al., 2023a; Qu et al., 2025) represent an important next validation step for extending the general applicability of the proposed platform. Differences in surface chemistry across EV types are expected to affect labeling efficiency and will be systematically addressed in future cross-source validation studies. Research on OMIEC channel materials (Dai and Yue, 2024; J. Kim et al., 2024; Zeglio et al., 2024) and integration into advanced iontronic circuit architectures (Ghittorelli et al., 2018; Romele et al., 2020; Yang et al., 2024) could further enhance performance, reinforcing the system potential as a robust, scalable tool for in-line quality control in EV production.

CRediT authorship contribution statement

Giulia Frusconi: Writing – original draft, Methodology, Investigation, Formal analysis, Conceptualization. **Angelo Musicò:** Resources, Investigation. **Andrea Zendrini:** Resources, Investigation. **Zsolt M. Kovács-Vajna:** Supervision, Investigation. **Lucia Paolini:** Resources, Investigation. **Paolo Bergese:** Validation, Supervision, Funding acquisition, Conceptualization. **Fabrizio Torricelli:** Writing – review & editing, Writing – original draft, Validation, Supervision, Funding acquisition, Conceptualization.

Declaration of competing interest

The authors declare that they have no known competing financial interests or personal relationships that could have appeared to influence the work reported in this paper.

Acknowledgements

The authors G.F., Zs.M.K-V., and F.T. acknowledge the financial support of the projects: “Tecnologie portatili e protocolli innovativi per la diagnosi ultrasensibile di *Xylella fastidiosa* direttamente in piante e vettori” (1LIVEXYLELLA), funded by Ministero dell'agricoltura, della sovranità alimentare e delle foreste, “Research actions for reducing the impact on agricultural and natural ecosystems of the harmful plant pathogen *Xylella fastidiosa*” (REACH-XY), C.U.P. B93C22001920001, funded by legge di bilancio del 30 dicembre 2021, n. 234, and “Smarcap”, funded by Ministero dello Sviluppo Economico (MISE) now Ministero delle Imprese e del Made in Italy (MIMI), Fondo per lo sviluppo di tecnologie e applicazioni di intelligenza artificiale, blockchain e internet of things, project FTE0000034, C.U.P. B87H21012300008. The authors A.M., A.Z., L.P., and P.B., acknowledge the financial support of the project “Muscle tissue extracellular vesicles: novel biomarkers for sepsis related Intensive Care Unit Acquired Weakness (ICU-AW)”, project i.d. RF-2021-12375279, Ricerca Finalizzata 2022, Ministero della Salute.

Appendix B. Supplementary data

Supplementary data to this article can be found online at https://doi.org/10.1016/j.biosx.2026.100755.

Data availability

The data that support the findings of this study are available from the corresponding author upon reasonable request.

References

Ahmed, W., Mushtaq, A., Ali, S., Khan, N., Liang, Y., Duan, L., 2024. ACS Biomater. Sci. Eng. 10, 5960–5976.
An, J., Park, Hyunjun, Kim, Jinmyeong, Park, Hanbin, Kim, T.-H., Park, C., Kim, Jeonghyun, Lee, M.-H., Lee, T., 2023. ACS Sens. 8, 3174–3186.
Armstrong, J.P.K., Holme, M.N., Stevens, M.M., 2017. ACS Nano 11, 69–83.
Belleri, P., Pons i Tarrés, J., McCulloch, I., Blom, P.W.M., Kovács-Vajna, Z.M., Gkoupidenis, P., Torricelli, F., 2024. Nat. Commun. 15, 5350.
Bhatta, R., Han, J., Liu, Y., Bo, Y., Lee, D., Zhou, J., Wang, Y., Nelson, E.R., Chen, Q., Zhang, X.S., Hassaneen, W., Wang, H., 2023. Nat. Commun. 14, 8047.

Cea, C., Zhao, Z., Wisniewski, D.J., Spyropoulos, G.D., Polyravas, A., Gelinas, J.N., Khodagholy, D., 2023. Nat. Mater. 22, 1227–1235.
Chen, Z., Ding, X., Wang, J., Guo, X., Shao, S., Feng, K., 2025. Angew. Chem. Int. Ed. 64, e202423013.
Ciferri, M.C., Bruno, S., Rosenwasser, N., Gorgun, C., Reverberi, D., Gagliani, M.C., Cortese, K., Grange, C., Bussolati, B., Quarto, R., Tasso, R., 2024. ACS Appl. Bio Mater. 7, 827–838.
Comfort, N., Cai, K., Bloomquist, T.R., Strait, M.D., Ferrante Jr., A.W., Baccarelli, A.A., 2021. JoVE J., 103791
Dai, H., Yue, W., 2024. Adv. Eng. Mater. 26, 2301860.
Deshmukh, S.K., Khan, M.A., Singh, S., Singh, A.P., 2021. ACS Omega 6, 1773–1779.
Feng, J., Xiu, Q., Huang, Y., Troyer, Z., Li, B., Zheng, L., 2023. Adv. Mater. 35, 2207826.
Feng, K., Shan, W., Wang, J., Lee, J., Yang, W., Wu, W., Wang, Y., Kim, B.J., Guo, X., Guo, H., 2022. Adv. Mater. 34, 2201340.
Feng, X., Iliuk, A., Zhang, X., Jia, S., Shen, A., Zhang, W., Hu, L., Tao, W.A., 2023a. Anal. Chem. 95, 2812–2821.
Feng, X., Jia, S., Ali, M.M., Zhang, G., Li, D., Tao, W.A., Hu, L., 2023b. J. Proteome Res. 22, 2516–2524.
Feng, X., Shen, A., Zhang, Wei, Jia, S., Iliuk, A., Wang, Y., Zhang, Wenke, Zhang, Y., Tao, W.A., Hu, L., 2025. Nat. Protoc. 20, 1057–1081.
Frusconi, G., Kovács-Vajn, Z.M., Blom, P.W.M., Gkoupideni, P., Torricelli, F., 2024a. Adv. Mater. Technol. 10, 2401440.
Frusconi, G., Kovács-Vajna, Z.M., Torricelli, F., 2024b. Adv. Mater. Technol., 2400301
Gegenschatz, S.A., Chiappini, F.A., Teglia, C.M., Muñoz de la Peña, A., Goicoechea, H.C., 2022. Anal. Chim. Acta 1209, 339342.
Ghittorelli, M., Lingstedt, L., Romele, P., Crăciun, N.I., Kovács-Vajna, Z.M., Blom, P.W. M., Torricelli, F., 2018. Nat. Commun. 9, 1441.
Gkoupidenis, P., Zhang, Y., Kleemann, H., Ling, H., Santoro, F., Fabiano, S., Salleo, A., van de Burgt, Y., 2023. Nat. Rev. Mater. 9, 134–149.
Granelli, R., Alessandri, I., Gkoupidenis, P., Vassalini, I., Kovács-Vajna, Z.M., Blom, P.W. M., Torricelli, F., 2022. Small 18, 2108077.
Granelli, R., Demartis, V.M., Frusconi, G., Kovács-Vajna, Z.M., Torricelli, F., 2025. Adv. Sci., e08872
Guo, K., Grünberg, R., Ren, Y., Chang, T., Wustoni, S., Strnad, O., Koklu, A., Díaz-Galicia, E., Agudelo, J.P., Druet, V., Castillo, T.C.H., Moser, M., Ohayon, D., Hama, A., Dada, A., McCulloch, I., Viola, I., Arold, S.T., Inal, S., 2024. Adv. Sci. 11, 2306716.
Hendrix, A., Lippens, L., Pinheiro, C., Théry, C., Martin-Jaular, L., Lötvall, J., Lässer, C., Hill, A.F., Witwer, K.W., 2023. Nat. Rev. Methods Primers 3, 56.
Herrmann, I.K., Wood, M.J.A., Fuhrmann, G., 2021a. Nat. Nanotechnol. 16, 748–759.
Herrmann, I.K., Wood, M.J.A., Fuhrmann, G., 2021b. Nat. Nanotechnol. 16, 748–759.
Hong, C., Ndukaife, J.C., 2023. Nat. Commun. 14, 4801.
Hu, S., Feng, X., Liu, K., Xie, Y., Xu, J., Zhou, B., Sun, L., Liu, B., Liu, M., Bai, X., Xu, L., Hu, L., Song, H., Dong, B., 2025. ACS Sens. 10, 8885–8894.
Huang, W., Chen, J., Yao, Y., Zheng, D., Ji, X., Feng, L.-W., Moore, D., Glavin, N.R., Xie, M., Chen, Y., Pankow, R.M., Surendran, A., Wang, Z., Xia, Y., Bai, L., Rivnay, J., Ping, J., Guo, X., Cheng, Y., Marks, T.J., Facchetti, A., 2023. Nature 613, 496–502.
Di Iorio, D., Rameshbabu, S., Bruijns, B., Movilli, J., Skolimowski, M., Huskens, J., 2022. Adv. Mater. Interfac. 9, 2200282.
Jeong, S., Park, J., Pathania, D., Castro, C.M., Weissleder, R., Lee, H., 2016. ACS Nano 10, 1802–1809.
Ji, J., Gao, D., Wu, H.-Y., Xiong, M., Stajkovic, N., Latte Bovio, C., Yang, C.-Y., Santoro, F., Tu, D., Fabiano, S., 2025. Nat. Commun. 16, 4334.
Kim, H., Won, Y., Song, H.W., Kwon, Y., Jun, M., Oh, J.H., 2024. Adv. Sci. 11, 2306191.
Kim, J., Pankow, R.M., Cho, Y., Duplessis, I.D., Qin, F., Meli, D., Daso, R., Zheng, D., Huang, W., Rivnay, J., Marks, T.J., Facchetti, A., 2024. Nat. Electron. 7, 234–243.
Koutsouras, D.A., Torricelli, F., Blom, P.W.M., 2023. Adv. Electron. Mater. 9, 2200868.
Kwong Hong Tsang, D., Lieberthal, T.J., Watts, C., Dunlop, I.E., Ramadan, S., del Rio Hernandez, A.E., Klein, N., 2019. Sci. Rep. 9, 13946.
Lee, J., 2024. Brain Tumor Res Treat, vol. 12, p. 153.
Lieberth, K., Pavlou, A., Harig, D., Blom, P.W.M., Gkoupidenis, P., Torricelli, F., 2023. Adv. Mater. Technol. 8, 2201697.
Lieberth, K., Romele, P., Torricelli, F., Koutsouras, D.A., Brückner, M., Mailänder, V., Gkoupidenis, P., Blom, P.W.M., 2021. Adv. Healthcare Mater. 10, 2100845.
Mathew, D.G., Beekman, P., Lemay, S.G., Zuilhof, H., Le Gac, S., van der Wiel, W.G., 2020. Nano Lett. 20, 820–828.
Nguyen, P.H.D., Jayasinghe, M.K., Le, A.H., Peng, B., Le, M.T.N., 2023. ACS Nano 17, 5187–5210.
Pham, T.C., Jayasinghe, M.K., Pham, T.T., Yang, Y., Wei, L., Usman, W.M., Chen, H., Pirisinu, M., Gong, J., Kim, S., Peng, B., Wang, W., Chan, C., Ma, V., Nguyen, N.T.H., Kappei, D., Nguyen, X., Cho, W.C., Shi, J., Le, M.T.N., 2021. J. Extracell. Vesicles 10, e12057.
Qu, S., Yang, S., Xu, Q., Zhang, M., Gao, F., Wu, Y., Li, L., 2025. Adv. Sci. 12, 2406496.
Ramadan, S., Lobo, R., Zhang, Y., Xu, L., Shaforost, O., Kwong Hong Tsang, D., Feng, J., Yin, T., Qiao, M., Rajeshirke, A., Jiao, L.R., Petrov, P.K., Dunlop, I.E., Titirici, M.-M., Klein, N., 2021. ACS Appl. Mater. Interfaces 13, 7854–7864.
Rashid, R.B., Ji, X., Rivnay, J., 2021. Biosens. Bioelectron. 190, 113461.
Ridolfi, A., Brucale, M., Montis, C., Caselli, L., Paolini, L., Borup, A., Boysen, A.T., Loria, F., Van Herwijnen, M.J.C., Kleinjan, M., Nejsum, P., Zarovni, N., Wauben, M. H.M., Berti, D., Bergese, P., Valle, F., 2020. Anal. Chem. 92, 10274–10282.
Rivnay, J., Inal, S., Salleo, A., Owens, R.M., Berggren, M., Malliaras, G.G., 2018. Nat. Rev. Mater. 3, 17086.
Romele, P., Ghittorelli, M., Kovács-Vajna, Z.M., Torricelli, F., 2019. Nat. Commun. 10, 3044.
Romele, P., Gkoupidenis, P., Koutsouras, D.A., Lieberth, K., Kovács-Vajna, Z.M., Blom, P. W.M., Torricelli, F., 2020. Nat. Commun. 11, 3743.
Saleh, A., Koklu, A., Uguz, I., Pappa, A.-M., Inal, S., 2024. Nat. Rev. Bioeng. 2, 559–574.
Salvigni, L., Nayak, P.D., Koklu, A., Arcangeli, D., Uribe, J., Hama, A., Silva, R., Hidalgo Castillo, T.C., Griggs, S., Marks, A., McCulloch, I., Inal, S., 2024. Nat. Commun. 15, 6499.
Sarkar, T., Lieberth, K., Pavlou, A., Frank, T., Mailaender, V., McCulloch, I., Blom, P.W. M., Torricelli, F., Gkoupidenis, P., 2022. Nat. Electron. 5, 774–783.
Scinto, S.L., Bilodeau, D.A., Hincapie, R., Lee, W., Nguyen, S.S., Xu, M., am Ende, C.W., Finn, M.G., Lang, K., Lin, Q., Pezacki, J.P., Prescher, J.A., Robillard, M.S., Fox, J.M., 2021. Bioorthogonal chemistry. Nat. Rev. Methods Primers.
Shen, A., Feng, X., Wang, D., Liu, Y., Zhang, K., Wang, J., Li, Y., Ali, M.M., Hu, L., 2024. Anal. Chim. Acta 1309, 342699.
Spitzberg, J.D., Ferguson, S., Yang, K.S., Peterson, H.M., Carlson, J.C.T., Weissleder, R., 2023. Nat. Commun. 14, 1239.
Tenchov, R., Sasso, J.M., Wang, X., Liaw, W.-S., Chen, C.-A., Zhou, Q.A., 2022. ACS Nano 16, 17802–17846.
Traberg, W.C., Uribe, J., Druet, V., Hama, A., Moysidou, C., Huerta, M., McCoy, R., Hayward, D., Savva, A., Genovese, A.M.R., Pavagada, S., Lu, Z., Koklu, A., Pappa, A., Fitzgerald, R., Inal, S., Daniel, S., Owens, R.M., 2023. Adv. Healthcare Mater. 12, 2301194.
Tran, H.L., Zheng, W., Issadore, D.A., Im, H., Cho, Y.-K., Zhang, Y., Liu, D., Liu, Y., Li, B., Liu, F., Wong, D.T.W., Sun, J., Qian, K., He, M., Wan, M., Zeng, Y., Cheng, K., Huang, T.J., Chiu, D.T., Lee, L.P., Zheng, L., Godwin, A.K., Kalluri, R., Soper, S.A., Hu, T.Y., 2025. ACS Nano 19, 28021–28109.
Usman, W.M., Pham, T.C., Kwok, Y.Y., Vu, L.T., Ma, V., Peng, B., Chan, Y.S., Wei, L., Chin, S.M., Azad, A., He, A.B.-L., Leung, A.Y.H., Yang, M., Shyh-Chang, N., Cho, W. C., Shi, J., Le, M.T.N., 2018. Nat. Commun. 9, 2359.
Wang, L., Wang, D., Ye, Z., Xu, J., 2023. Adv. Sci. 10, 2300552.
Wang, S., Zhang, L., Wan, S., Cansiz, S., Cui, C., Liu, Y., Cai, R., Hong, C., Teng, I.-T., Shi, M., Wu, Y., Dong, Y., Tan, W., 2017. ACS Nano 11, 3943–3949.
Welsh, J.A., Goberdhan, D.C.I., O'Driscoll, L., Buzas, E.I., Blenkiron, C., Bussolati, B., Cai, H., Di Vizio, D., Driedonks, T.A.P., Erdbrügger, U., Falcon-Perez, J.M., Fu, Q.L., Hill, A.F., Lenassi, M., Lim, S.K., Mahoney, M.ÿ.G., Mohanty, S., Möller, A., Nieuwland, R., Witwer, K.W., 2024. J. Extracell. Vesicles 13, e12404.
Welsh, J.A., Van Der Pol, E., Arkesteijn, G.J.A., Bremer, M., Brisson, A., Coumans, F., Dignat-George, F., Duggan, E., Ghiran, I., Giebel, B., Görgens, A., Hendrix, A., Lacroix, R., Lannigan, J., Libregts, S.F.W.M., Lozano-Andrés, E., Morales-Kastresana, A., Robert, S., De Rond, L., Tertel, T., Tigges, J., De Wever, O., Yan, X., Nieuwland, R., Wauben, M.H.M., Nolan, J.P., Jones, J.C., 2020. J. Extracell. Vesicles 9, 1713526.
Wu, G., Zhao, Y., Li, X., Ali, M.M., Jia, S., Ren, Y., Hu, L., 2023. TrAC, Trends Anal. Chem. 159, 116930.
Wu, W., Feng, K., Wang, Y., Wang, J., Huang, E., Li, Y., Jeong, S.Y., Woo, H.Y., Yang, K., Guo, X., 2024. Adv. Mater. 36, 2310503.
Xiang, B., Zhang, S., Zhao, I.S., Gan, X., Zhang, Y., 2025. Adv. Sci. 12, 2503027.
Xu, G., Jin, J., Fu, Z., Wang, G., Lei, X., Xu, J., Wang, J., 2025. Signal Transduct. Targeted Ther. 10, 255.
Xu, L., Liang, Y., Xu, X., Xia, J., Wen, C., Zhang, P., Duan, L., 2021. Bioengineered 12, 7929–7940.
Yang, W., Feng, K., Ma, S., Liu, B., Wang, Y., Ding, R., Jeong, S.Y., Woo, H.Y., Chan, P.K. L., Guo, X., 2024. Adv. Mater. 36, 2305416.
Yang, W., Ma, S., Gámez-Valenzuela, S., Jeong, S.Y., Lee, J., Cai, H., Zhu, R., Liu, B., Woo, H.Y., Kim, B.J., Wang, S., Chan, P.K.L., Guo, X., Feng, K., 2025. Advanced Materials e12070.
Yin, T., Xu, L., Gil, B., Merali, N., Sokolikova, M.S., Gaboriau, D.C.A., Liu, D.S.K., Muhammad Mustafa, A.N., Alodan, S., Chen, M., Txoperena, O., Arrastua, M., Gomez, J.M., Ontoso, N., Elicegui, M., Torres, E., Li, D., Mattevi, C., Frampton, A.E., Jiao, L.R., Ramadan, S., Klein, N., 2023. ACS Nano 17, 14619–14631.
Zeglio, E., Wang, Y., Jain, S., Lin, Y., Avila Ramirez, A.E., Feng, K., Guo, X., Ose, H., Mozolevskis, G., Mawad, D., Yue, W., Hamedi, M.M., Herland, A., 2024. Adv. Mater. 36, 2302624.